
Cellular Automata Models of Volcanism



NEWCASTLE UNIVERSITY

SCHOOL OF MATHEMATICS AND STATISTICS

Olivia Butters (B1009535)

MMath Report

Supervisors: Dr Graeme Sarson and Dr Paul Bushby

May 2015

Abstract

Throughout the centuries, volcanoes and earthquakes have had devastating effects on populations across the globe. Due to their chaotic and unpredictable nature, observatories around the world have been established to monitor seismic activity. However, due to a lack of historical data, patterns and trends, especially with regards to volcanic activity, are difficult to determine. The aim of this dissertation therefore has been to use advances in technology, to recreate, expand and develop idealised cellular automata models with an aim to gaining a better understanding of some of the key processes and statistics exhibited by volcanoes. The model considers the rise of magma through the chamber of a volcano to be permitted in discrete batches, through cracks caused by stress within the rocks. Once pre-established models had been verified, an adaptation of the model was created, observing the interrelationship between the stress and magma fields. It was discovered that incorporating a dependence on the stress field by the magma field, resulted in an axial symmetry, a physical property of volcanoes that could be utilised in future work on these models.

Contents

1	Introduction	1
1.1	Self-Organised Criticality	1
1.2	Cellular Automata Models	2
1.3	The Burridge-Knopoff Spring Model	3
2	Earthquakes - The Properties of the OFC Model	5
2.1	Plate Tectonics - Earthquakes	5
2.2	The Model	5
2.3	Boundary Conditions	7
2.4	Gutenberg Richter Law	8
3	Magma transport via a Fracturing Mechanism	12
3.1	Introduction	12
3.2	The Model	12
3.3	Reservoir to surface connection	16
3.4	Stationary state	17
4	Analysis of Results	19
4.1	Complications	19
4.2	Probability Distribution	19
4.3	Inter-Eruption Times	21
4.4	Axial Symmetry	23
5	Degassing and Styles of Volcanic eruptions	25
5.1	Physical Degassing	25
5.2	The Model	25
5.3	Types of Eruption	26
5.4	The Probability Distribution of Eruptions with regards to gas loss	28
6	Magma Induced Fractures	31
6.1	Introduction	31
6.2	Implementation	31
6.3	Implications to Eruption Statistics	32
6.4	Implication on the Stress Field	34
6.5	Subsequent Implications on the Magma Field	36
7	Conclusions and Future Directions	38

1 Introduction

Throughout the centuries, volcanoes and earthquakes have had devastating effects on populations across the globe. Due to their chaotic and unpredictable nature, observatories around the world have been established to monitor seismic activity and other diagnostics with the hope of providing advanced warnings of major events. Mathematics plays an important role in monitoring techniques, as data from various precursor quantities is collected, checked, cross referenced and analysed in order to discover trends or anomalies. As developments in technology continue to increase, more and more methods for potentially identifying catastrophic events are becoming available. The aim of this work was to build upon a model that was originally produced by Piegari *et al.* in 2008^[1] which looks at developing cellular automata models exhibiting self-organised criticality, to recreate mathematical properties relating to volcanic activity.

A volcanic eruption is defined to be an event where molten lava and fragmental material are ejected.^[2] Eruptions range widely, from explosive eruptions to effusive eruptions, large in magnitude to small in magnitude, persistent activity to dormant volcanoes. These variations in magnitude and duration from volcano to volcano have made cataloging and recording volcanic data hard. Therefore by building up idealised models of the physical processes involved in volcanic eruptions, the aim is to gain a better understanding of some of the key process and statistics exhibited by volcanoes.

The model written by Piegari *et al.* for volcanism was developed from earlier works on self-organised criticality by Bak, Tang and Wiesenfeld,^[3] and further extensions of that work, produced by Olami, Feder and Christensen^[4] on cellular automata models. In each of these cases, although the papers set out their principles and findings, the actual computer models and the empirical data produced by the authors was not available. As a consequence it was necessary to write the programs again and then rerun the models, in order to confirm the results of the newly programmed model and verify these against the findings set out in the published papers.

Therefore, all results in this report have been established following rewrites and replications of the previous models of others, and only when this work had been verified, was it possible to develop the model further and test new additional variables.

1.1 Self-Organised Criticality

In 1988, Bak, Tang and Wiesenfeld (BTW) introduced the concept of Self-Organised Criticality: “when a natural system is perturbed from a marginally steady state, it will evolve back to a state of marginal stability”.^[5] They postulated that the underlying mechanism behind a diverse number of natural phenomena, such as river networks, superconductors, the spread of epidemics and earthquakes, can be described by Self-Organised Criticality.

In their original paper, BTW considered a system comprising of many individual components, driven by random local perturbations. They suggested that, under what can be very general conditions, the individual components evolve globally into an organised state with a complex but general structure. By observing complex systems (that is those which are not controlled by one characteristic, such as time or length), with complex responses and outcomes, they demonstrated that the properties shown in the system can be described by simple power laws.^[6] Examples of these power laws are observed in both earthquake and volcano analysis. The most famous of these is the Gutenberg-Richter Law which describes a relationship between the number of earthquakes per unit time of a given magnitude, and the Omori law, regarding the distribution of aftershocks. In Section 2.4, the Gutenberg-Richter Law will be considered in more detail and it will prove a useful test to determine the realistic characteristics of the model.

1.2 Cellular Automata Models

The concept of cellular automata models was introduced in 1966 by John Von Neumann,^[7] and it provides a powerful technique for modelling complex systems. Although it was initially developed to model the behaviour of a human brain, it has since been applied to various systems in nature, such as earthquakes and volcanoes. The technique has proven to be very effective in modelling some physical systems, as it can capture the global behaviour of the system arising from the combined behaviour of the local action of its (individually very simple) components.

A very simple description of the model can be given using a one-dimensional array of cells, where at time $t = 0$, each component of the grid is assigned an initial state. Other than the initial configuration of the system, there is no input into the system, hence the model is autonomous. Over a period of discrete time steps, the state of each individual cell is updated, based on a function commonly known as a “local rule”, that relates the current state of the cell to the state of its neighbouring cells. In the one-dimensional case, the neighbouring cells are those to the left and right of the original cell within the array. The states of the cells are completely determined at each point in time by this rule, and so the system proceeds deterministically over a set number of time steps.^[8]

The initial model created by BTW was based upon modelling a sandpile using a Cellular Automaton Model to illustrate numerically how the system can organise into a critical state. Grains of sand were dropped onto the individual cells of the array, with the gradient of each cell, that is the number of grains of sand, determining the stability of the pile. The moment the number of grains rises above a critical value, the pile slips and the grains are distributed to the neighbouring cells, determined by the local laws. Within this model the number of grains of sand is discrete and the model is conservative within the centre of the grid, whilst at the edges, boundary conditions determine the conservative nature. However, looking ahead to implementing this model to represent

seismic activity, the dynamic variable of the system is the local force or stress acting on a block, which is not discrete. During an event the energy released dissipates and so the conservation of this variable, both within the model and at the boundary, must be considered since the total stress is not necessarily redistributed to surrounding cells. The earthquake model implemented in this paper is known as the OFC model, after its creators, Olami, Feder and Christensen and, in Section 2.4 the conservative nature of the OFC model will be examined, taking into consideration the effects of different boundary conditions.

1.3 The Burridge-Knopoff Spring Model

In 1967 the Burridge-Knopoff Spring model was developed. It simulates a two-dimensional slider-block model which, whilst appearing very simple and uniform, is deterministically chaotic.

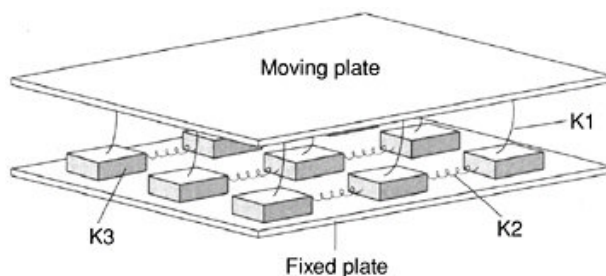


Figure 1: The Burridge-Knopoff spring model.^[9]

Relating Figure 1 to the basic cellular automata model, it can be seen that the cells of the model are represented here by a finite number of blocks, connected to their four neighbours by springs K_2 and K_3 . Each of the blocks are resting on a fixed plate, whilst a second plate is resting on top of them, attached by the springs denoted K_1 . The top plate has momentum and, over time, this plate moves slowly causing stresses to build up as friction between the blocks and the fixed plate counteracts the force trying to move the individual blocks. As time elapses, the static frictional force needed to counteract the force imposed by the top plate, increases until a moment is reached when it is overcome by the force of momentum and one of the blocks slips. The result of this causes energy to dissipate to the neighbouring cells, the amount being determined by the simple local rules. So from the cellular automata model, the state of each cell represents the current stress on that block.

There are however both key similarities and differences between the cellular automata model and the slider-block model, and they are summarised in the table below:

Cellular Automata	Slider-Block Models
Discrete lattice of sites in space	Discrete lattice of sites in space
Evolve in discrete time steps	Evolve continuously in time
Each site takes on a finite set of possible values	Each site takes continuous values of displacement and stress
The value of each site evolves according to the same rules	The value of each site evolves according to the same rules
The evolution of a site depends only on a local neighbourhood of sites	Upon failure a sliding block interacts with all blocks which are in motion simultaneously

Table 1: Comparison between Cellular Automata and Slider-Block Models.^[5]

The Cellular Automata model has been shown to exhibit the key properties of Self-Organised Criticality and therefore this very simple idea forms the basis upon which the earthquake and volcano models are built. In Section 2.1 a physical interpretation of this model will be discussed, relating the event of a block slipping to the occurrence of an earthquake. Therefore, the initial model will reflect that produced by Olami, Feder and Christensen (OFC),^[4] which is an idealised version of the Burridge-Knopoff spring model.

A two-dimensional version of this model, namely a grid (matrix) of finite size, made up of uniform cells, each connected to 4 neighbouring cells will be used. The state of each cell within the model will represent the stress at a specific point on the grid at a specific time. Initially the grid will represent an arbitrary section of the Earth's crust, orientated along a particular fault plane, as a model is developed to produce statistical outcomes of earthquakes and ground movement. However, from Section 3 onwards, the grid will represent a vertical cross section of a volcano, stretching from the magma reservoir to the surface.

2 Earthquakes - The Properties of the OFC Model

2.1 Plate Tectonics - Earthquakes

Statistics show that the most common earthquakes occur at the boundaries of rigid tectonic plates. The surface of the Earth is not static and therefore as the plates drift, the relative motion occurs across a narrow network of edges. As two plates push against each other, the friction between the rocks prevents the plates from sliding freely and steadily over time, causing stress to build up and the ground to deform and accumulate strain. As the stress increases over what can be hundreds or even thousands of years, the strain on the rock builds until eventually it will fracture along a weakened fault plane; within a matter of seconds, energy can be released in the form of heat, noise and seismic waves as the plates slide. This fracture which initiates locally, is very quickly propagated over a large distance of the fault surface.^[7] Building upon the visual representation of this idea as shown in Figure 1, the model, in a simplified form, was created by Olami, Feder and Christensen in 1991,^[4] to demonstrate some of the key physical properties of earthquake analysis. In order to later produce a cellular automata model for volcanism, the OFC model was first written and reproduced using Fortran, and the results from 10^7 simulations analysed, cross-examined and presented graphically using Matlab.

2.2 The Model

In order to simulate the OFC model and map the spring-block model to a cellular automata model, grids of varying size, $L \times L$, were considered, where L was chosen in order to compare, contrast and understand results. The grid was defined by an array where each block of the grid had coordinates (i, j) , with $1 \leq i \leq L$ and $1 \leq j \leq L$, for $i, j \in \mathbb{N}$.

The dynamic variable labelled f , represents the local force/stress being applied to a given block of the Burridge-Knopoff model. At time $t = 0$ each of these blocks were assigned a random value $f_{i,j}$, which was somewhere between 0 and the threshold value f_{thresh} , that is, the point at which the stress is greater than the opposing force resulting in the block slipping. Throughout this paper $f_{thresh} = 1$.

For convenience in this model, the elastic constants connecting neighbouring blocks (represented in Figure 1 by K_2 and K_3) were set to be equal, that is the isotropic case. Once the system was established, the basic state was then perturbed at a constant rate, until one of the values rose above the threshold value. This was determined by the equation,

$$f_{i,j} \rightarrow f_{i,j} + \nu \Delta t, \quad (2.1)$$

where Δt represents the elementary time period and ν is a constant. As the system was slowly perturbed, the behaviour followed a set of simple rules described in the algorithm

in Figure 2 below. For simplicity the direction of motion was restricted to be in the direction of the moving plate.

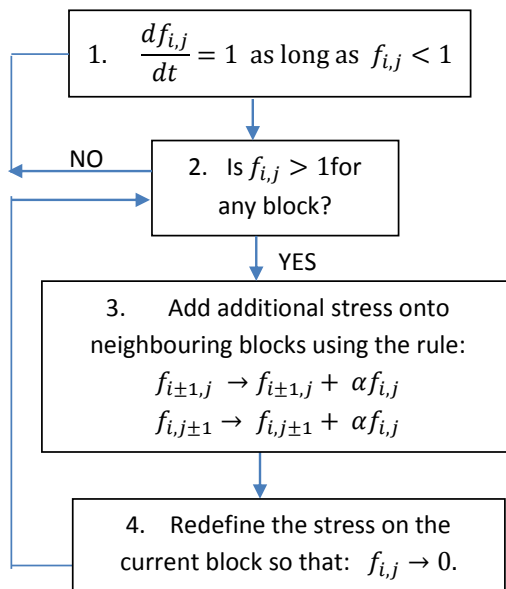


Figure 2: A flow chart picturing the algorithm of the OFC model.

The algorithm above shows the simple local rules that determine the transfer of stress as a block slides. Step 1 shows a long-term driving force acting at a constant rate whilst the blocks are stable and the rate of change of the stress, ν , has been normalised to unity. However, as a block slides a proportion of the stress determined by the constant α is allocated to the neighbouring blocks, whilst the stress on the original block is set to zero. Due to the fact that each cell has a maximum of 4 neighbours, $\alpha \in [0, 0.25]$ since it is dependent on the strength of the springs connecting the blocks. In order to generate a realistic model, a non-conservative case was considered, using $\alpha < 0.25$. Hence only a fraction of the stress was distributed to each neighbour and the fraction of the stress dissipated was given by,

$$(1 - 4\alpha)f. \quad (2.2)$$

It is also important to take into consideration the time element of the model, which can split into 2 distinct phases, namely,

1. **The External Driving Rate** - This refers to the periods of a constant driving force, i.e. step 1 in Figure 2. In physical terms this relates to the time period between earthquakes, which can range from minutes to hundreds of years.

2. **The Internal Relaxation Rate** - This refers to the length of time of the earthquake itself which can last a matter of seconds.^[6]

In order to determine the time between events, following each recorded earthquake, the cell with the maximum stress was located. Each cell was identically perturbed at a constant rate and so the cell with the maximum stress will be the next block to slip. Therefore, using the threshold value of 1, the amount needed to cause the onset of a future event was calculated to be:

$$\delta F = 1 - \maxval(f), \quad (2.3)$$

(taking the value of ν from Equation (2.1) to tend to zero). This not only determined the time between each event but also produced a faster running code since, rather than adding a small perturbation to each cell at each time step and then checking for a block slipping, the value of δF was added to each of the values of stress, resulting in the occurrence of another event. The distribution of times between events is one test of the accuracy of the model. This involves comparing the results of the model to the Omori Law, which shows a power law relating to the frequency of aftershocks occurring after major earthquakes.^[6]

2.3 Boundary Conditions

Given grids of finite size, it is important to consider appropriate boundary conditions on the blocks around the edge. There are three different methods that can be implemented each with their various advantages and disadvantages.

Rigid frame boundary conditions are based on the idea that the blocks at the boundaries are connected to a rigid frame in exactly the same way in which they are connected to their neighbouring blocks. This can be implemented using a grid size of $(L+1) \times (L+1)$. During the initial assignment of random values to each cell, those on the rigid frame remain zero and therefore won't be involved in an earthquake. As stress is distributed to the neighbouring cells, step three of Figure 2, the cells on the rigid frame are set back to zero. This results in a loss of stress at the boundaries since, along with the stress dissipated as shown in Equation (2.2), there is a further loss of

$$\frac{\alpha f_{i,j}}{4}, \quad (2.4)$$

lost at the edges and

$$\frac{\alpha f_{i,j}}{2}, \quad (2.5)$$

lost at the corners.

A second method of addressing boundary conditions is commonly known as free boundary conditions. This approach is that the blocks on the edge of the grid only have three neighbours and those at the corners two, whilst the rest have four. Therefore when a share of stress is distributed to neighbouring cells following a slip, those at the boundary receive a different amount to those in the middle. In order to implement this a concept of connectivity was introduced, denoted by C , representing the number of neighbours a cell has. Using this method, Step three of Figure 2 was rewritten to read:

$$f_{i\pm 1,j} \rightarrow f_{i\pm 1,j} + \frac{4\alpha}{C} \quad (2.6)$$

$$f_{i,j\pm 1} \rightarrow f_{i,j\pm 1} + \frac{4\alpha}{C} \quad (2.7)$$

where $C = 4$ in the centre of the grid, $C = 3$ at the edges and $C = 2$ at the corners. In comparison to the rigid frame boundary conditions, this second method allows the stress to be conserved across the boundaries.

The final method for treating boundary conditions is referred to as periodic boundary conditions. In order to remove the issue of conservation of stress, this idea is formulated in such a way that the blocks on the edge of the grid are connected to those on the opposite edge which results in zero energy loss. However, in relation to this paper, these boundary conditions were not considered to be appropriate for the physical interpretation of both earthquakes and volcanoes, since finite sided systems are required and therefore such an extended system will not be sensible. Throughout this report, rigid-frame boundary conditions will be applied to the model being considered, in accordance with both the OFC model and the later Piegari model.

2.4 Gutenberg Richter Law

Plate boundaries, where the majority of earthquakes occur, are complex and it is often difficult to identify one single fault line as there can be branching faults that add complexity to the system.^[5] Nevertheless, in 1954, Gutenberg and Richter developed an equation showing a simple relation for $N(m)$ - the number of earthquakes of a given magnitude m per unit time:

$$\log_{10}(N(m)) = a - bm, \quad (2.8)$$

where a, b are constants. This law is useful because it can be applied not only to local events but also global ones. However, the parameter b has been recorded to have a wide range of values, $0.8 < b < 1.54$, varying from region to region and also with respect to the size of the earthquake.

The energy released during an earthquake increases exponentially with its magnitude, that is,

$$\log_{10} E = c + dm, \quad (2.9)$$

where d changes depending on the size of the earthquake and c is a constant. Using this a power law can be generated, related to the size distribution measured, that looks at earthquakes with a minimum energy, E against the number of observed earthquakes.

$$N(E_0 > E) \sim E^{-b/d} = E^{-B}. \quad (2.10)$$

The exponent B can vary between $0.8 < B < 1.05$ for different fault lines.^[4]

In order to show that the model produces the self-organised power law shown in the Gutenberg Richter Law, a graph representing the probability density distribution of the size of earthquakes was obtained. If the model emulates this law, it would suggest that the process that causes earthquakes is largely scale invariant.^[10] This would imply that the large-scale statistical properties of earthquakes is insensitive to the specific environmental details and therefore can be represented by simple models that duplicate the basic statistical properties shown in real life data.

In the 1992 paper of Olami, Feder and Christensen^[4] they recorded the result their model produced regarding the probability density distribution of the size of earthquakes, and so their paper was ideal for checking the validity of the model. The statistics produced are based on 10^9 results, using a fixed value of α , namely 0.2. In order to analyse the results varying grid sizes were used, $L = 15, 25, 35$ and 50 . In keeping with the OFC paper, rigid frame boundaries were applied to the system. This resulted in the figure shown below.

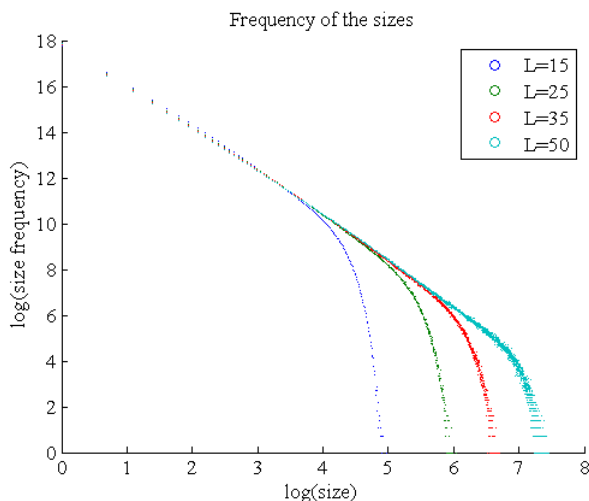


Figure 3: Probability density of having an Earthquake of Energy E , for varying L .

The power law described in Equation (2.10) can be rewritten in order to describe the probability density function,

$$P(E_0 = E) \sim E^{-(1+B)}. \quad (2.11)$$

In Figure 3, Olami, Feder and Christensen postulated that the gradient, that is the power law exponent shown in Equation (2.11), was $B \approx 0.91$. However, in their later paper^[11] they produced a table which stated that for $\alpha = 0.2$, $B = 0.89 \pm 0.1$. The result obtained by the model was $B = 0.909$ with a standard deviation of 0.015. Therefore it can be seen that the model is producing plausible values of an important statistic from actual recorded earthquake data.

Further checks on the model can be made by using the same law to determine the role of the conservative nature of the system. Varying the value of α , it is possible to determine whether the self-organised property shown above is maintained for the model with varying levels of conservation. Running the model, this time fixing $L = 35$, using rigid boundary conditions and varying α for the values above, the sizes of 10^8 earthquakes were obtained producing the probability density plot below.

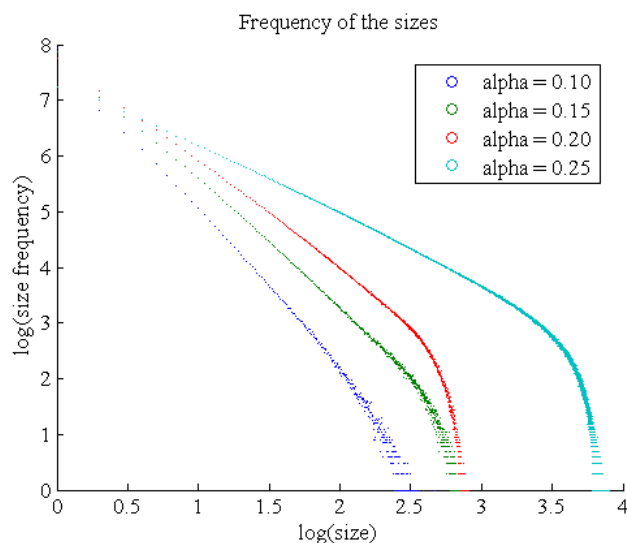


Figure 4: Simulation results for the probability density of having an Earthquake of Energy E , varying α .

The gradients of these curves and the comparative results produced by Olami, Feder and Christensen can be seen in Table 2 below.

Model	$1 + B$ (Given OFC results)	$1 + B$ (Simulated Results)
$\alpha = 0.10$	2.72 ± 0.10	2.747
$\alpha = 0.15$	2.22 ± 0.10	2.226
$\alpha = 0.20$	1.89 ± 0.10	1.895
$\alpha = 0.25$	1.22 ± 0.05	1.241

Table 2: The critical exponents of the system produced by Olami *et al.* and the recreated OFC model, with errors indicated.^[11]

The results produced in Figure 4 are within the confidence levels shown in Table 2. From this it can be deduced that this continuous, non-conservative model exhibits a self-organised criticality. It is important to note that when changing the value of α , although it does have an impact on the exponent, it does not alter the critical nature of the model.

There are two important things to note here:

1. By basing the model being written on pre-established work by Olami, Feder and Christensen, it has been possible to verify the algorithm used. Also by cross comparing obtained results, the code produced during this project was verified with respect to the work of others.
2. On a wider scale, through agreement with the OFC model results and common laws regarding the physical phenomena, the model used can be seen to be in agreement with observed data from earthquakes across the globe.

Therefore having achieved verification of the replication of the OFC model, the model can now be adapted and developed for an assessment of volcanic activity.

3 Magma transport via a Fracturing Mechanism

3.1 Introduction

In order to create a cellular automata model for volcanism, a variant of the OFC model was used, building upon the underlying concept that: “*Volcanoes can be regarded as large scale natural magma-fracturing experiments repeated over a long period of time.*”^[12] Recent discoveries have suggested that the transport of magma is facilitated through stress fields within the magma chamber of a volcano, and, along with the natural buoyancy of magma, it is allowed to ascend towards the surface through crack networks in the fractured rock. Previously the cellular automata model has represented a horizontal section of the Earths crust, recording at each time period the size and distribution of ground movement across the grid. In order to employ the model for volcanic purposes, the grid will now represent a vertical cross-section of a volcano with the OFC model tracking the areas of fractured rock within the magma chamber.

For clarity, the volcano was schematised into three different regions, the magma reservoir, the magma chamber and the surface.

1. **The Magma Reservoir** - This is the feeder from the source of the magma into the chamber of the volcano. (In the majority of cases this will not be involved within an eruption, however there are a small number of large eruptions, such as the Soufriere Hill in Monserrat, where input from the reservoir is involved within the eruption, and therefore this is something that must be taken into consideration when implementing the model.^[13])
2. **The Magma Chamber** - Within the chamber, the magma that is fed in from the reservoir is transported and stored, as it migrates through the rock towards the surface moving through connected fractured cells. During ascent, if the magma stops at any point then the magma loses some of its volatiles. This will be considered in greater detail in Section 3.3.
3. **The Surface** - The surface is the outlet for eruptions. Once magma reaches the surface, an eruption occurs and the size is dependent on the volume of magma lost from the system.

Therefore the model being developed builds on the premise that, rather than there being a connection from the surface of the earth to a deep pressurised magma chamber via a continuous conduit, the magma is injected into the system in small batches, where magma is seen to be a diffusive field, permitted to rise through self-organised cracks in the rocks.

3.2 The Model

To adapt the model, the principal idea shown in Figure 1 and the algorithm shown in Figure 2 were applied to determine the location of fractures appearing in the formation

of the magma chamber as the pressure builds up in the rocks. Again a square lattice of size $L \times L$ was used, only this time a further space and time dependent field was incorporated, denoted $n_{i,j}$ to represent the presence of magma. This model focused on describing closed conduit volcanoes, i.e. volcanoes with infrequent eruptions, with inter-eruption times up to tens of thousands of years.

Throughout the simulations the 2 fields, $f_{i,j}$ and $n_{i,j}$, were recorded regularly at various time steps, since both arrays can be mapped onto the same grid in order to determine the location of both stresses in the rock and the presence of magma within the chamber at a given moment in time. Initially the array $n_{i,j}$ was set to zero since at the start of the simulations no magma was within the system. However, as magma began to rise through the chamber, the field $n_{i,j}$ was updated, with those cells containing magma represented by a 1. Further details of additional properties of magma that were introduced into the model are discussed in Section 5, requiring a change from an integer array $n_{i,j}$ to a real array.

A visual representation of this model can be seen in Figure 5 which shows a schematic, simplified view of the initial model over 4 consecutive time periods, using a grid of size 8×8 . Defining the top row to represent the layer of rock adjacent to the surface, the bottom row to represent the magma reservoir of width $N = L/4$ (which is filled with magma throughout the whole simulation) and the rest of the grid to be the magma chamber, made it possible to model the idealised rise of magma.

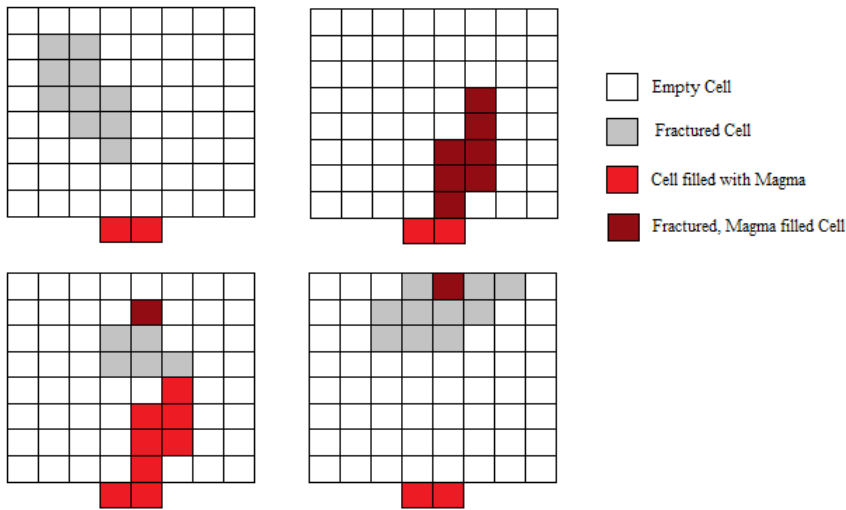


Figure 5: Schematic cartoon of four stages of the model.

In order to determine how the magma rises from the reservoir to the surface, three simple flow diagrams of the model were created, relating to the four stages of the model above. The first of these describes the rise of magma from the reservoir into the chamber. This algorithm was applied at each time step when stresses in the rock appeared.

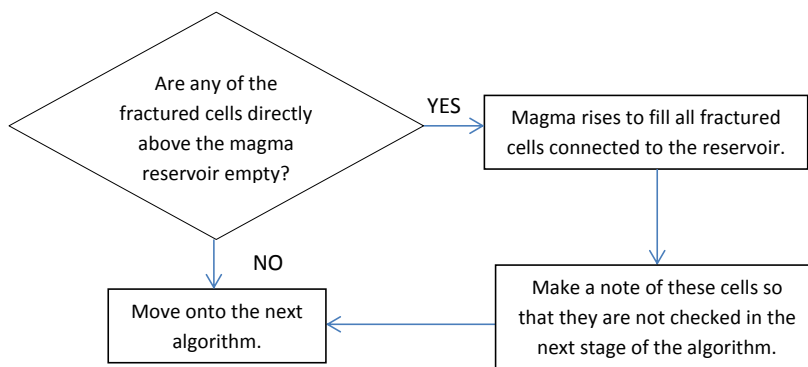


Figure 6: Stage 1 - Flow diagram picturing the rise of magma from the reservoir into the chamber.

The top left hand grid of Figure 5 shows stress in the rock causing a fracture to appear; however due to the relative position of the fracture being located far away from the reservoir, no magma was permitted to enter the system. In the example shown by the top right hand square, fractured cells appear adjacent to the reservoir and so magma was permitted to enter all connected cells. By recording the cells involved within this magma movement, the model has no need to check these cells again for magma movement since all connected fractured cells to the reservoir have been accounted for.

In their 2011 paper, Piegari *et al.* provided a flow diagram determining the movement of magma within the chamber. However, in order to refine the model and better determine how the magma moved, a few variants of the method were tested in order to determine which ran most efficiently, before the algorithm in Figure 7 was created.

- **Vertical Movement** - After a check to see if magma could rise up one cell, the next step initially was to perform a check on the possible horizontal movement of the batch of magma. However, this did not allow the buoyancy of the magma to dominate and so to refine the model, first the magma was allowed to rise as high (and through as many cells) as it could, before any horizontal movement was even considered. If the magma then moved a cell either to the left or right the vertical check would be performed again, before any further horizontal motion could occur.
- **Horizontal Movement** - It was not possible to determine easily from the flow chart below provided by Piegari *et al.* how many times the model would allow for horizontal movement. Due to the probabilistic nature of the horizontal movement, the magma could be moving backwards and forwards continuously within the magma routine. Therefore it was decided to limit the horizontal movement between cells. After checking for vertical movement, the magma would be allowed to move one place horizontally, followed by a subsequent check on the vertical movement. If again magma was permitted to move upwards, then a further horizontal

movement one place across would be permitted, until no further vertical movements could occur. This would then mark the end of the magma movement with the current fractured event and so another ‘Earthquake’ run would be required. In the second 2011 paper by Piegari *et al.*^[14] they applied restraints to the horizontal movement in order to implement a central conduit, thereby assuming an axial symmetry. Due to the fact that this is in a later paper, this was implemented after the results of the first 2011 paper were verified.

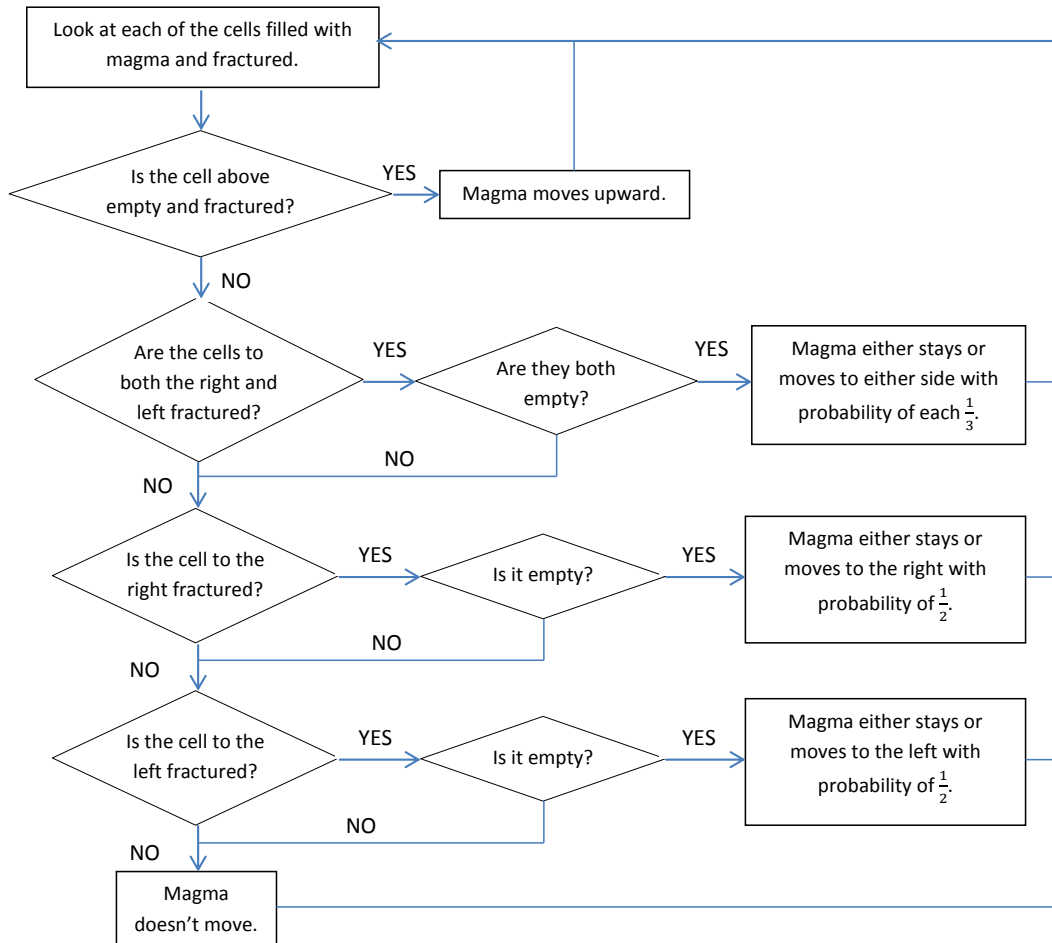


Figure 7: Stage 2 - Flow diagram picturing the movement of magma within the chamber.

This algorithm sequentially considers each cell in turn as it sweeps through the grid and a simple application of this algorithm can be seen in the bottom left hand square of Figure 5. One of the magma filled cells is fractured and adjacent to a cluster of fractured cells, hence the magma present can diffuse into the fractured cluster with buoyancy resulting in an upward bias. The rest of the magma filled cells which are not

fractured remain as they are. Following each application of the check for vertical movement of magma in Figure 7, a check was performed to determine whether any magma had reached the surface (the top row of the grid). If it had, then the following eruption algorithm was called.

The third and final algorithm focused on the surface of the volcano and recorded eruption events. It is described by the flow chart in Figure 8 and is illustrated by the bottom right hand square of Figure 5. In order to determine when an eruption occurs, this algorithm is called once a cell adjacent to the surface is filled with magma.

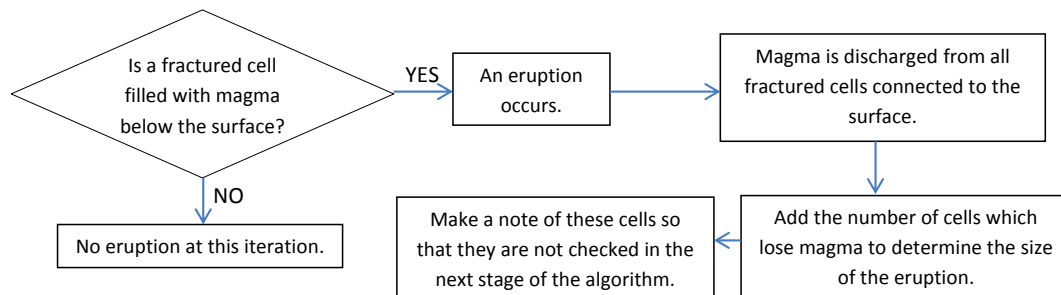


Figure 8: Stage 3 - Flow diagram picturing an eruption of varying sizes.

By keeping track on which cells are involved within an eruption the model becomes more time effective, as once an eruption had taken place these cells could be ignored, as the simulation continued to loop over the remaining cells within the chamber determining further magma movement. In the special cases where the fractured cells connect the reservoir to the surface, the algorithm described in Figure 7 is bypassed, and an eruption occurs directly following the rise of magma from the reservoir into the system.

3.3 Reservoir to surface connection

When the cracks within the magma chamber remain relatively small, magma moves in small batches up from the reservoir towards the surface, resulting in relatively small volumes of magma in any ensuing eruptions. However, it is also important to take into consideration the special cases when the reservoir and surface are connected by a continuous set of fractures, allowing a rapid and continuous flow of a very large volume of magma that drains the chamber.

This is a realistic property of certain volcanic eruptions, and in the 1980 paper written by Wilson *et al.* on explosive volcanic-eruptions, they state that an explosive eruption is “*initiated by the formation of a fracture connecting the magma to the surface.*”^[15]

In the case of Figure 9 the reservoir is connected to the surface by a wide conduit resulting in an eruption of high velocity. It shows an event where the fractured cells

stretch from the reservoir to the surface. The lighter shaded cells represent those filled with magma, but not fractured. The darker red cells are those fractured cells, filled with magma that can move between connected fractured cells. This snapshot was taken at a time step when the algorithm described in Figure 6 had occurred, resulting in magma rising to the surface from the reservoir through fractured cells, but prior to the eruption algorithm being called, which flushes the magma out of the system.

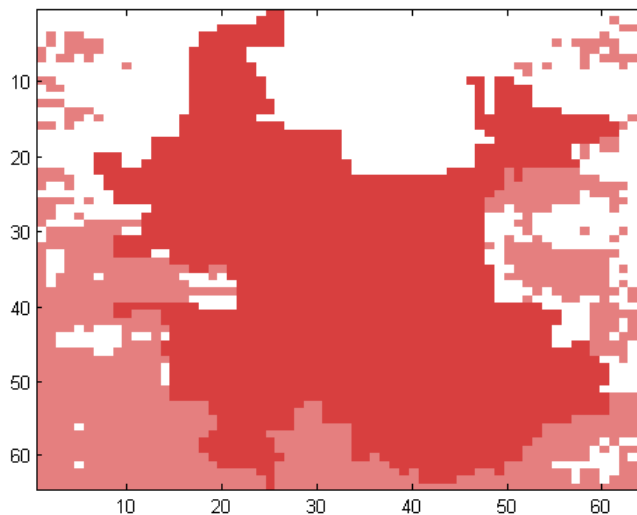


Figure 9: Reservoir to surface eruption.

It was decided that in order to prevent the model getting trapped on a continuous flow of magma rising from the reservoir to the surface, only one batch of magma would be permitted to rise into the system from the reservoir, and once this had been flushed out of the fractured cells connected to the surface, that event would be terminated and the whole process would start again. In physical terms the eruption ends when either the pressure results in the collapse of the chamber walls, preventing the rise of additional magma, or the magma supply is exhausted.^[13]

3.4 Stationary state

To analyse the results effectively, it is important to consider the time it takes for the system to evolve to a stationary state. At the start of simulations, there is no magma present within the grid, resulting in a much larger time period between eruptions, until the system evolves to a steady state. Therefore in order to determine the transient period until the system reaches the steady state, the mean magma level per grid point was recorded following an eruption. Then plotting the mean eruptions as a function of the eruption number and calculating the mean values of magma, increasing percentages of the starting data were removed resulting in Figure 10.

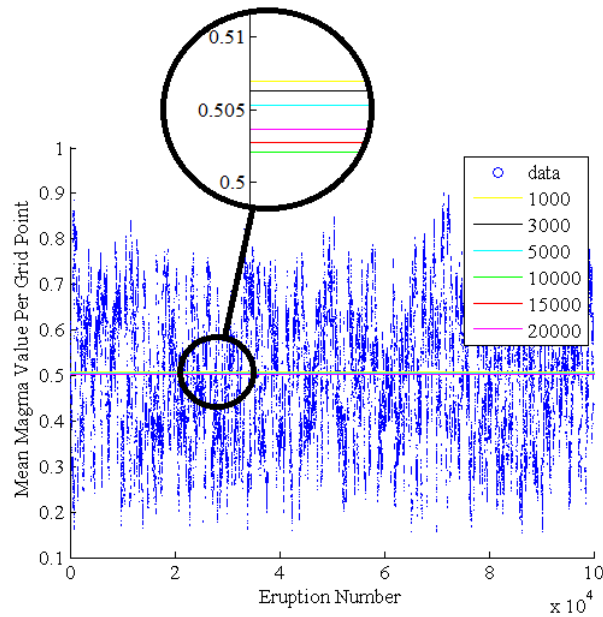


Figure 10: Mean Magma value per grid point following 10^5 eruptions where the values in the legend refer to the number of data points removed.

It can be seen from the graph that the mean value of magma within the grid fluctuates rapidly following an eruption and regardless of the percentage of data removed at the beginning of the simulation, all the values are within less than 0.02 of each other, and do not tend to one specific value. In comparison to the size of the fluctuating data, the difference in the mean values across the 10^5 eruptions excluding various percentages of data is very small and, therefore, it is very difficult to determine at which point the model reaches a stationary state.

Subsequently it was decided that the first 5000 pieces of data would be ignored from the observations as, seen above, anything less than this would result in a very small but slightly higher mean magma value than observed once the system has reached a steady state.

4 Analysis of Results

4.1 Complications

Unlike empirical earthquake records, there has been no analogous system for recording volcanic eruptions over the centuries, with most recorded events being limited to descriptive documentations of major events, such as the eruption of Vesuvius in AD79 which had catastrophic effects. There is a distinct lack of records regarding smaller events and often the data is incomplete and lacking in essential quantitative data. In light of this it is very hard to determine statistical properties of volcanic eruptions, similar to the Gutenberg-Richter Law found for earthquakes. Consequently within the last century a composite estimate of past eruptions was proposed, known as the Volcanic Explosivity Index (VEI).^[16] It is comprised of semi-quantitative data based on small pockets of data and written reports of events. This lack of quantitative data presents a significant obstacle when wanting to compare the model against historical data and known properties of eruptions. However, some trends have been found and in more recent times, eruptions occurring across the globe have been well documented.

4.2 Probability Distribution

In order to analyse the results produced by the model, the initial aim was to reproduce the results published by Piegari *et al.* in 2008.^[1] In a similar way to the OFC model, they started off by looking at the probability distribution of eruptions in relation to their volume, V , via a log-log scale and using varying grid sizes. The results they obtained are displayed in Figure 11, and a value -1.6 was quoted for the gradient of their curves.

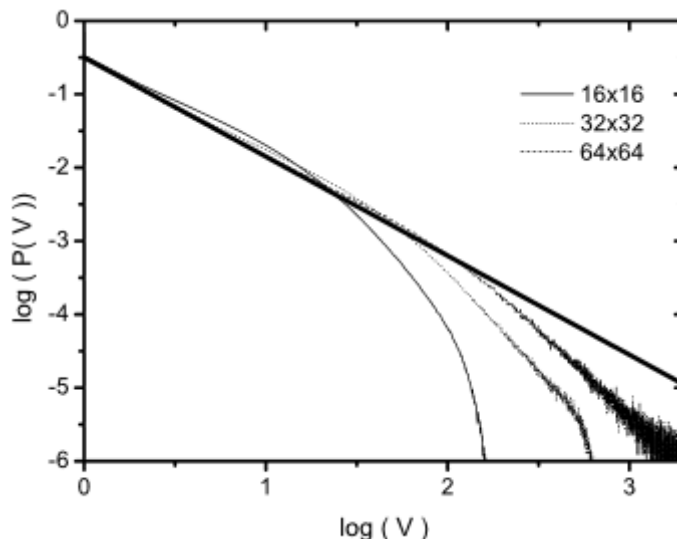


Figure 11: Probability distribution, $P(V)$ of eruptions generated by Piegari *et al.*^[1]

However, looking closely at their graph and calculating the gradient manually, the gradient shown is closer to a value of -1.36 , which does not appear to support their quote for the exponent of the power law fit.

In Figure 12 below is the comparative plot produced by the statistics of 10^7 eruptions from the model. A very similar distribution with a power law behaviour can be seen, characterising a large proportion of the data. The difficulty with attempting to replicate the resultant power law quoted, is that no further information was available regarding the limits chosen when calculating the line of best fit. Therefore the data was collected by applying rigid frame boundary conditions, in line with those used in the 2008 paper, and the fit was determined within limits $[0,1]$. The resultant power law fit had the value -1.488 .

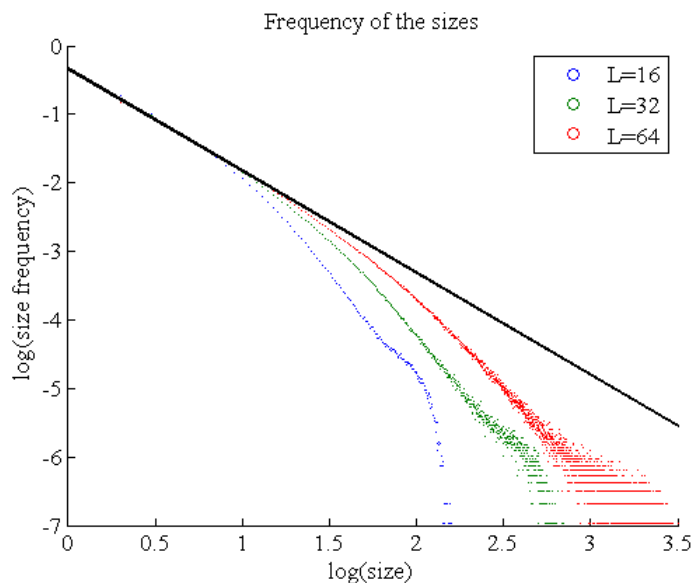


Figure 12: Probability distribution, $P(V)$ of eruptions, as a function of the volume V on a log-log scale.

As can be seen in Figure 12, the system evolves into an organised state displaying a power law relation between the log frequency of eruptions of differing sizes. Despite the lack of tangible data as outlined in Section 4.1, more than 4 decades of recorded data from active volcanoes has been recorded,^[2] and catalogue records also show a power law regime relating the number of eruptions and their Volcanic Explosivity Index. Another factor made evident in the figure is the grid size dependence and the cut off of the power law. It can be observed that the larger the value of L , the longer the power law regime.

4.3 Inter-Eruption Times

Another key feature in the statistical analysis of volcanoes is the time between the occurrence of eruptions. Observing patterns in the data, or noticing any correlations, is essential when monitoring or attempting to predict future volcanic activity. Determining whether eruptions are random processes or are correlated is therefore essential. In order to glean as much information about the time between events, the cumulative distribution $P(> t)$ of repose times was examined, defining the time difference to be from the start of one event to the start of the subsequent event. The aim was to determine whether a Poisson process is controlling the occurrence of eruptions, i.e., do the inter-eruption times follow an exponential distribution?

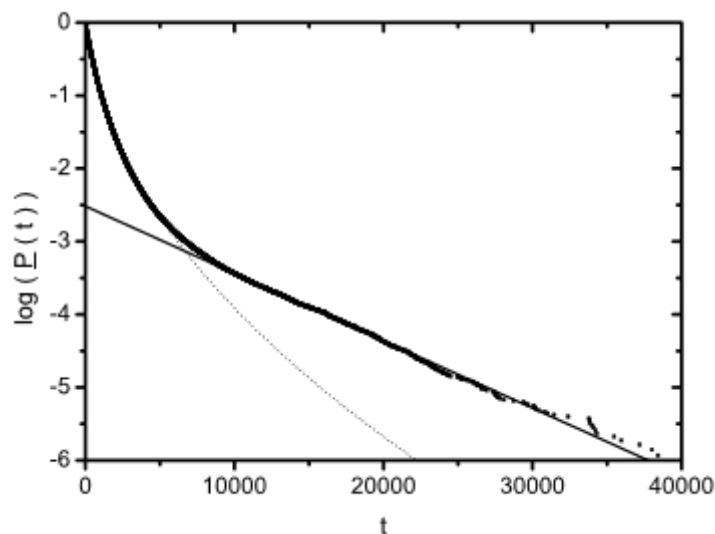


Figure 13: The cumulative distribution, $P(t)$ of inter-eruption times larger than t (in units of ν^{-1}) as a function of t in a log-linear scale produced by Piegari *et al.*^[1]

Figure 13 shows that a change point at $t \approx 7500$ identified two regions of importance. For large values of t , the figure shows an exponential behaviour, whereas for small values of t a stretched exponential was observed. From this they inferred that the probability of eruption is often not dependent on the prior history of the volcano. Within their paper the exponential and stretched exponential fits were presented but the results were dependent on the value of ν .

The result in Figure 13 was based upon t being calculated in units of ν^{-1} , where ν is the constant in Equation (2.1) determining the speed of the driving rate. However, in Section 2.2 the value of $\nu \rightarrow 0$ was determined by pinpointing the cell with maximum stress and calculating,

$$1 - \maxval(f), \quad (4.1)$$

in order to determine the external driving rate of the system. Therefore in order to determine the scale of the model, contact was made with Ester Piegari and further clarification was sought. She stated that within their model they “counted the steps necessary for magma to reach the surface”, which was interpreted to mean they produced an integer value representing the time between events by summing the values of Δt . This corresponds to the number of steps of ν needed for an eruption to occur. Considerable time was spent on adapting and altering the code with the hope of recreating their numerical results and, in the end it was decided that to be consistent with the OFC model, the time between events would be determined by summing the values of $1 - \maxval(f)$ needed to get from the onset of one earthquake to the beginning on the next. This was based on the method explained in the 1998 book by Henrik Jensen^[6] during the discussion and reproduction of the Omori Law regarding the aftershocks of earthquakes. He defined the time span between successive events to be denoted by Equation (4.1). This method produced Figure 14 with the scale of the graph determined by binning the data into 40000 bins to create the best possible comparison with Piegari *et al.*'s results.

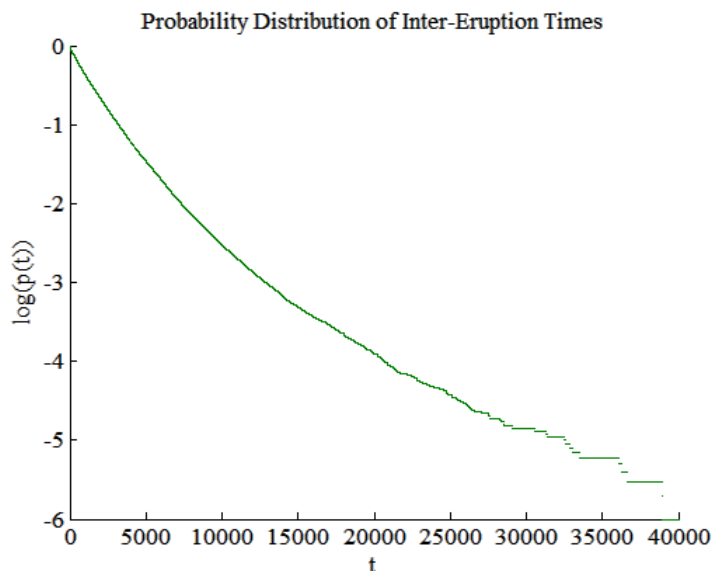


Figure 14: The cumulative probability distribution of inter-eruption times, calculated for 10^7 events.

Whilst in Figure 13 the cut off point between the stretched exponential and normal exponential is very pronounced, with the stretched exponential ranging over the values $[0 \ 8000)$, the point of change in Figure 14 is less clear, and the linear fit over the larger values of t less apparent.

Comparing the two figures above numerically, on a log-linear scale, both show that events occurring after a large inter-eruption time are far less probable. An attempt was made to reproduce the exponential behaviour for large t using the equation

$$P(t) \propto \exp(-t/\tau_1). \quad (4.2)$$

In Figure 13 Piegari *et al.* determined the gradient of the straight line between the values of approximately (8000 40000], resulting in $\tau_1 = 10^4$. Looking between the same limits on Figure 14, τ_1 was obtained to be 1.064×10^4 which, although seemingly relatively accurate, doesn't fit along the line as obviously as in Figure 13, as the data dips below the line of fit. The value of τ_1 was calculated between various limits, however the best comparative result was produced by the same limits as shown in Figure 13.

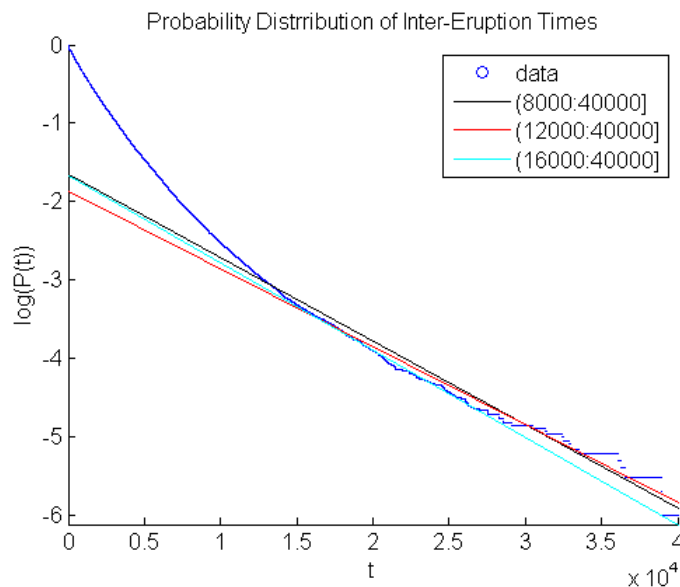


Figure 15: The cumulative probability distribution of inter-eruption times, calculated for 10^7 events.

Having spent a lot of time attempting to gain more concise results, it was decided to move on, especially since further adaptations to the model, such as the axial symmetry described in the next subsection, would change the shape of the inter-eruption time graph anyway.

4.4 Axial Symmetry

In later papers written by Piegari *et al.*^[17] they imposed an axial symmetry upon the top half of the grid. Volcanoes such as Vesuvius have the property that the magma chamber favours the a central path through which the magma can rise. This is prevalent in many cone-shaped volcanoes, and so within the model the aim is to limit the horizontal movement of the magma towards the flanks of the volcano. The impact of adding in this additional restraint has no effect on the geometry of the cracks, determined by the field $f_{i,j}$. Instead it required adapting the method portrayed in Figure 7, by restricting the movement within the field $n_{i,j}$ so that within the top half of the grid, horizontal

movement of magma is permitted if, and only if, it is towards the centre of the grid.

This restriction produced little change within the probability density distribution of eruption events, but a noticeable change occurred within the inter-eruption times of the resultant events.

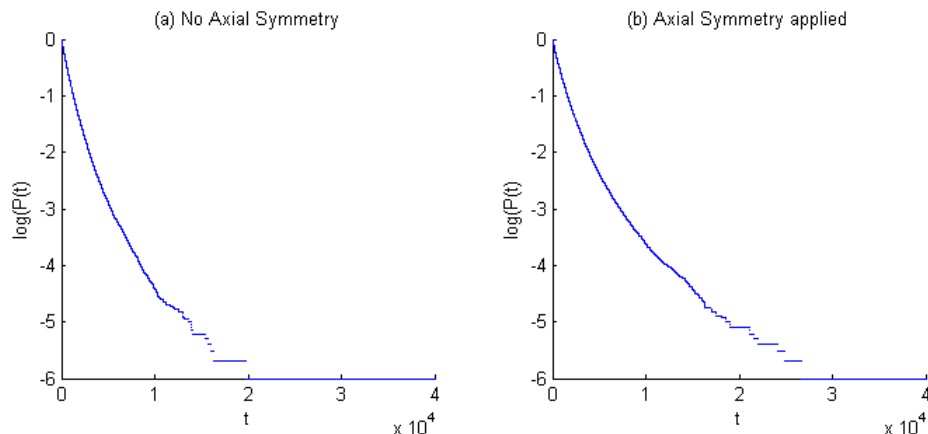


Figure 16: The cumulative probability distribution of inter-eruption times: (a) using no axial symmetry, and (b) using axial symmetry on the upper half of the grid. Statistics taken from 10^6 eruptions.

Running the simulation for a model implementing axial symmetry and the model used in previous sections, Figure 16 was produced. As can be seen from the Figure 16(b), there is a much more obvious stretched exponential in the cumulative distribution than that shown in Figure 16(a). This implies there is a greater occurrence of events with longer inter-eruption times.

Although the physical properties of inter-eruption times can be analysed for both the model with and without the addition of an axial symmetry, the cross-comparison with results produced by Piegari *et al.* is more inconclusive. This is due to the fact that their only published analysis of the inter-eruption times is in their 2011 paper, whereas in the 2013 paper, with the axial symmetry applied, no further analysis of the times were discussed. However, since the results show a more conclusive agreement with laws regarding the physical phenomena, the model is deemed sufficiently accurate to move on to further adaptations.

5 Degassing and Styles of Volcanic eruptions

5.1 Physical Degassing

Volcanoes are very complex systems; whilst some display persistent activity with effusive eruptions (e.g. Mount Etna, Italy), others occur infrequently, in some cases after hundreds or thousands of years of apparent inactivity and erupt explosively (e.g. Mount St Helens, USA). Therefore, in order to encompass the varying explosive natures of volcanoes from around the globe, the model will now be adapted, following the idea outlined in Piegari *et al.* (2011),^[18] that once the magma has reached the local saturation pressure, it starts to exsolve water. This loss of water content is controlled throughout the magma chamber, by the pressure on the magma at varying depths. Incorporating this into the model, creates a physically more accurate model and, allows for the analysis of the probability of eruptions based on varying gas content, which is essential to understand in regards to the style of Volcanic eruptions.

As magma moves from high pressured depths towards the surface, it starts off with all the available volatiles being dissolved within the liquid magma. As it rises towards the middle of the chamber, the exsolution of volatiles occurs, resulting in a magma comprising of liquid and gas bubbles. As it reaches the surface the pressure acting on the magma reduces further and the magma is split into pyroclasts and released gases.^[15] Explosive eruptions are the most dangerous, destructive and powerful events of all volcanic activity. The physical process responsible for these events, and for the fragmentation of the magma ejected is poorly understood. This makes forecasting and monitoring the conditions of the volcano in the lead up to events difficult, as is determining the resultant explosive nature of the eruption.^[19] Therefore in this section, the varying water content of magma residing at different depths will be implemented, and the statistics of both effusive and explosive events analysed.

5.2 The Model

The OFC model described in Section 2.2, and the subsequent additions made in Section 3.2, facilitated further adaptations to the array tracking the movement of magma, $n_{i,j}$. As before, an empty cell was defined with a value of 0, but the presence of magma could now be denoted with values ranging from $(1 - n_{loss})$ to 1, where n_{loss} represents the percentage of gas lost from the magma. For the initial model only the water content of the magma of the model was taken into account, determined by the relationship between the dissolved water concentrate, n_d , and the lithostatic pressure p for basalt, where the lithostatic pressure is the pressure caused by the weight of the overlying rock. This relationship is given by

$$n_d = 6.8 \times 10^{-8} p^{0.7}, \quad (5.1)$$

where the lithostatic pressure is calculated using

$$p = p_0 + g \int_0^z \rho(z) dz, \quad (5.2)$$

and $\rho(z)$ is the density of the rock at depth z . n_0 was defined to be the initial dissolved water content, whilst the value of n_d varies with the depth.^[17]

In order to replicate the results of the 2011 paper,^[18] the depth of the grid was set to be $h = 12\text{km}$, the gravity to be $g = 9.81$, the pressure at the surface to be $p_0 = 0$ and the constant rock density to be $\rho = 2700\text{kg/m}^3$. To implement this, 12000 (the depth in m) was divided by the total number of blocks from the reservoir to just below the surface, that is $L + 1$, and then multiplied by the number of the row to obtain the depth of each row. As before a magma reservoir at the bottom of the grid was created to be filled with saturated magma, where the value of $n_{i,j}$ in this section was denoted by a 1. The gas lost n_{loss} was calculated using the equation

$$n_{loss} = n_0 - n_d, \quad (5.3)$$

with an initial value of $n_0 \approx 6\%$. Therefore it was anticipated that if water was lost as the magma rises, then n_d gets smaller the closer it is to the surface. The water would be exsolved if and only if the magma stopped at any point in the model, (i.e. between earthquake events), with $n_{i,j}$ taking the value of $(1 - n_{loss})$ based on the depth at which it comes to rest. In this case n_{loss} could never be greater than 6%. Hence the value of the magma filled cells ranged from $0.94 < n_{i,j} < 1$, where 0.94 denoted magma without water near the surface and 1 the saturated magma found within the magma reservoir.

5.3 Types of Eruption

In the 2008 paper by Scandone *et al.*^[13] they looked at the role of the velocity of the magma in producing episodic and sustained eruptions, which are determined by the velocity of the magma as it rises through the chamber. They looked at four common cases regarding the ascent of magma, including both effusive and explosive eruptions dependent on the velocity of the magma, as can be seen in Figure 17 below.

In order to fully comprehend how these four common cases relate to the model, Figure 18 was created. It shows a visual representation of the varying types of eruption. Each grid represents a vertical cross section of a volcano, where the y-axis represents the depth of the chamber, and the x-axis the width. The fractured cells are represented by the grey cells and the magma cells by varying shades of reds and pink dependent on the gas content of the magma. The higher up the grid the magma stops, the lighter the shade of the magma. In a similar vein, the blue cells represent the cells of the array which are both fractured and filled with magma. (By varying the colour of the blue shades, it was easier to determine the water content of the magma present in the chamber.) Each of the four cases presented in the two figures are described below.

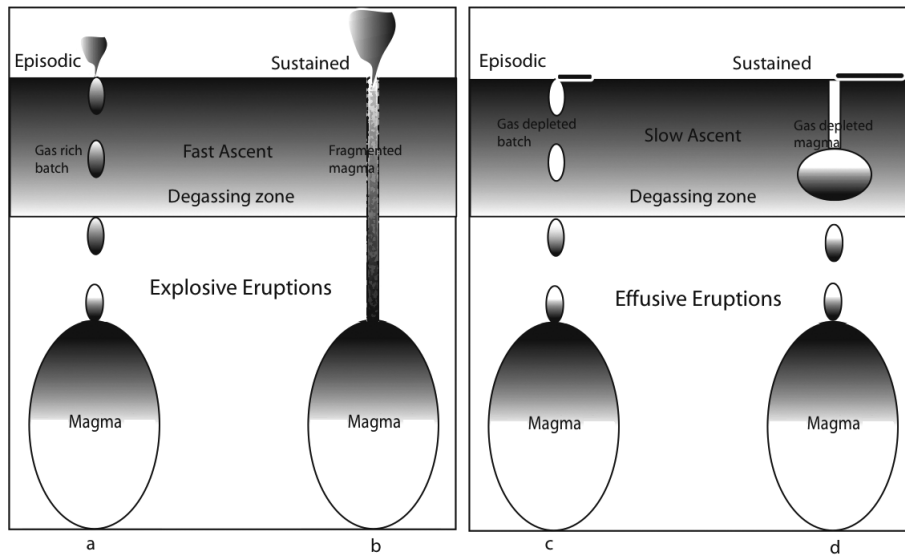


Figure 17: Scheme of magma ascent and eruptive mechanisms.^[13]

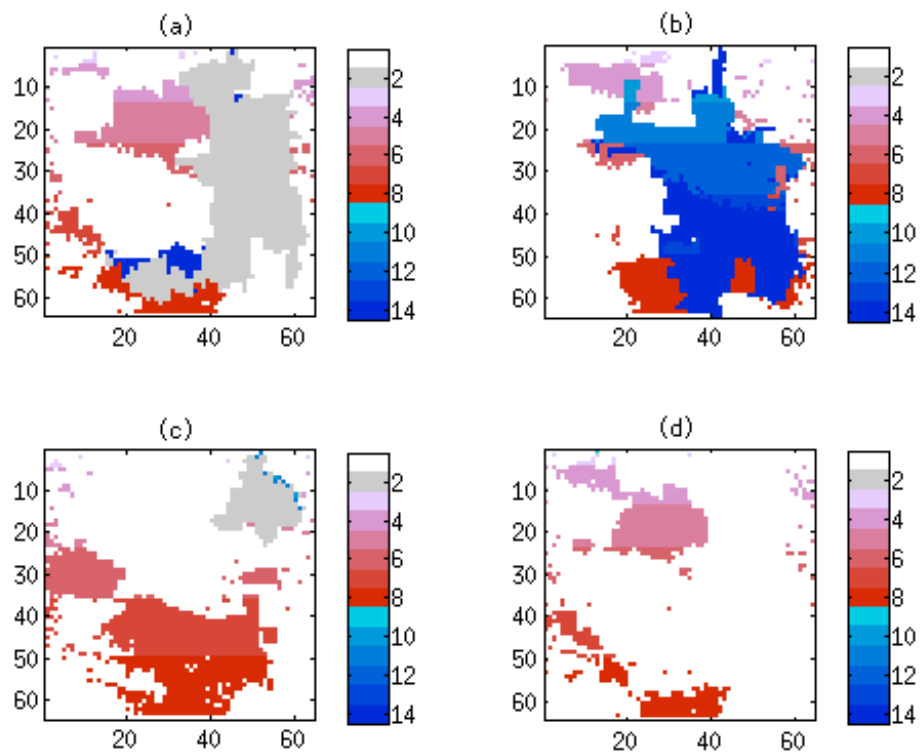


Figure 18: Comparative representations of eruptions produced by the model. The colour bar labels are arbitrary; see text for an explanation.

- (a) Figure 17(a) shows an episodic explosive eruption caused by small batches of gas filled magma reaching the surface. In Figure 18(a) it can be seen that these occur when deeper small batches of magma are connected to the surface via fractured cells. Therefore when magma containing a high water content is connected to the surface, it results in a relatively small but explosive eruption.
- (b) Figure 17(b) shows a sustained explosive eruption can be seen caused by a much lower region of the magma chamber (or the magma reservoir) being connected to the surface. At lower depths, the magma has a higher water content and so this results in a fast ascent of magma, and an explosive eruption. In the corresponding Figure 18(b), the fractured cells are connected to the surface from the reservoir, and a large amount of magma containing a high water content is erupted.
- (c) Figure 17(c) shows a slow ascent of magma, where the pressure has allowed the water content of the magma to drop, resulting in gas depleted batches. These batches result in effusive eruptions which have a short duration period. As seen in Figure 18(c), only a small amount of magma is erupted.
- (d) Figure 17(d) shows eruptions caused by the feeding of magma from a large shallow ‘reservoir’, resulting in an eruption. This required looking at individual eruptions and the distribution of magma within the grid to determine whether or not the magma is being fed to the surface via this reservoir, something which will not be considered here. Looking at Figure 18(d) however it could be interpreted that the pool of magma in the top left hand quarter of the grid is a secondary reservoir containing magma with a much lower gas content.

In order to determine the types of eruption, following an event volcanologists will calculate the Magma Discharge Rate by taking samples of the erupted magma and analysing its properties.

5.4 The Probability Distribution of Eruptions with regards to gas loss

Figure 19 presents the results of the simulations in the form of a histogram of the occurrence of eruptions with given percentages of gas loss. The results in accordance with Piegari *et al.* were generated using a grid of size 120×120 , collecting the number of eruptions of given gas loss into bins of equal width $\approx 0.1\%$. The graph shows a far greater probability of the occurrence of an eruption with the magma having almost completely lost its gas content, whilst at the other end of the spectrum, those eruptions with almost fully saturated magma are far rarer.

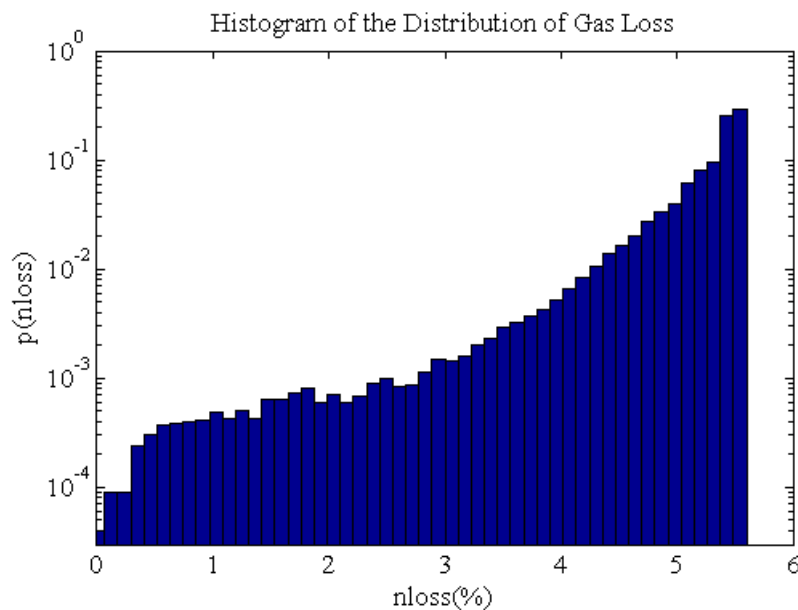


Figure 19: Distribution of 10^6 simulated eruptions grouped according to the percentage of gas loss.

The results appear to follow an approximately exponential distribution (the histogram produced is normalised and produced on a log-linear scale); that is events of increasing gas loss are exponentially more likely to occur than those of a much smaller gas loss. The histogram shows that events with no gas lost almost never occur (in regards to surface to reservoir eruptions, magma that resided within the grid before that time step will have lost gas and therefore 100% gas loss is extremely unlikely). Physically this is a reasonable result as large eruptions from volcanoes will have experienced gas loss to some extent.

Explosive eruptions, such as the recent eruption of Calbuco in Chile, are often characterised by large volumes of lava, accompanied by ash clouds and pyroclastic flows. This is the result of the dissolved gases within the magma escaping during the eruption and blasting rock and lava fragments into the atmosphere. Explosive eruptions often have lethal effects, whereas effusive eruptions are generally not particularly hazardous to humans^[20] (although in the case of the Calbuco eruption, nearby citizens were evacuated in sufficient time to avoid fatalities). The more common effusive eruptions are characterised by the outpouring of magma down the flank of a volcano. For example Kilauea volcano, which is almost constantly erupting, has lava flows commonly occurring down its flank. It is of paramount importance therefore, to develop an understanding of the different types of flow and their probabilities, due to the resultant impact they have on peoples lives.

Having made a qualitative comparison between the results produced by the code and that by Piegari *et al.* a more quantitative check was needed. Below in Figure 20 the

conditional probability was obtained for the size of events with gas loss $\geq 5.5\%$, where again the size of an event is defined to be the number of cells which lose magma during an eruption (Figure 8).

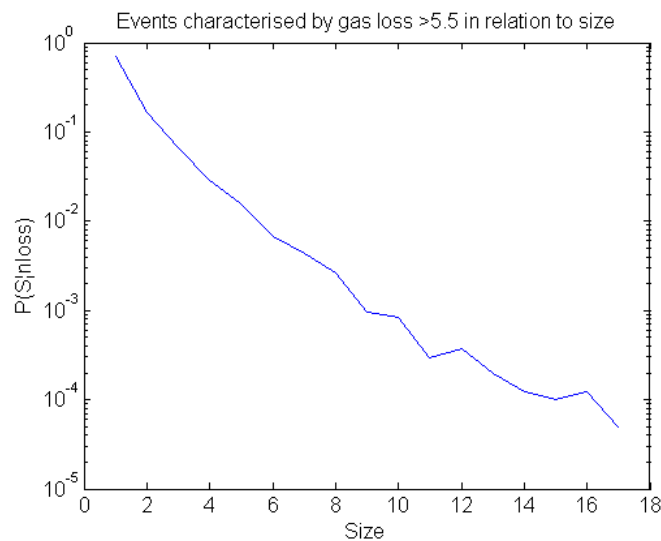


Figure 20: The conditional probability distribution of events of size S with $n_{loss} \geq 5.5\%$.

Figure 20 shows the conditional probability $p(S|n_{loss})$ of eruptions of size S with a gas loss n_{loss} of eruptions with $n_{loss} > 5.5\%$. That is, effusive eruptions, made up of magma that has stopped within the top cells of the grid, as shown in Figure 18(c). The significance of this graph is that effusive eruptions are relatively small in size with a range of the number of cells involved of only 0 – 17. This is in agreement with the result produced in Figure 5 of the 2013 Piegari paper.^[18]

Having now reproduced some of the key statistical features of volcanic eruptions in terms of gas loss and cross-analysed these results against those produced by Piegari *et al.*, the next step was to develop the model by looking at other physical properties of magma and the impact they have on eruptions.

6 Magma Induced Fractures

6.1 Introduction

Since deciding to develop the OFC model to incorporate a magma field, developments of the model have focused solely on variables that have a direct impact on the magma field $n_{i,j}$. These have included the gas loss, as discussed in Section 5, and the difference in density levels between the magma and surrounding rock which was evaluated in the 2013 paper by Piegari *et al.* Therefore in order to take a step away from, and further advance the work developed by Piegari, a new variable was considered that not only has an impact on the magma field $n_{i,j}$, but also on the stress field $f_{i,j}$. Prior to this point the stress field has been an independent variable, determined solely by the OFC model, whilst the magma field has been dependent on the location of fractures determined by the stress field. Within this section of the paper, the interrelationship of these variables will be considered.

The geophysical process of loading is complex, as stress can be caused by compression, tension or shear processes.^[21] Previously the role of the shear stress had been emphasised, based on the underlying principle behind the OFC model, of friction building up until it is overcome by the shear stress. However, other factors could be taken into consideration such as overpressure in the chamber, the weakening of the Earth's crust by corrosion^[17] or stress caused by the intrusion on magma. Within this report the last of these will be considered and the effects of this additional factor on the model will be analysed.

For magma to migrate through the chamber, it must exert enough stress to induce new fractures sufficiently large enough for the magma to continue its ascent.^[22] So as magma is injected into the system, the chamber deforms plastically and the pressure increases. As this happens fractures can appear as, in a similar way to the OFC model, a threshold value is reached and the pressure becomes too great. The resultant high pressure creates a compressive stress zone close to the cells of the grid where the magma is located, with a radial stress zone radiating out from the magma to surrounding cells. This additional pressure leads to further crack initiation and fracture growth.^[21]

6.2 Implementation

To implement this new, additional, physical concept into the model, the basic OFC model was adapted so that an additional amount of stress was added onto the magma filled cells (initially ignoring radial stress zones). At the end of an "earthquake event", the stress of those cells which had slipped and become fractured was reset to zero, as can be seen in Step 4 of Figure 2, due to the non-abelian nature of the model. Therefore when applying the OFC model to volcanic eruptions, as the magma rises, it stops in cells where the stress value of the block is zero. The magma can also reside in unfractured cells where the value of stress increases with the constant driving force defined in the

OFC model.

In order therefore to take into account additional stress caused by the magma filled blocks, Equation (2.3) was adapted. By splitting the grid into two, i.e. those cells with magma (regardless of the gas content) and those cells without magma, it was possible to calculate the maximum value of stress for both sets. These were determined by the two equations,

$$dt_{nomag} = 1 - \maxval(f_{nomag}), \quad (6.1)$$

$$dt_{mag} = \frac{1 - \maxval(f_{mag})}{1 + \delta}, \quad (6.2)$$

where f_{nomag} denotes the set of values of $f_{i,j}$ for those cells with no magma, and f_{mag} , those containing magma. The value of δ , represents a new model parameter, describing the fractional, additional stress occurring in the magma filled cells.

The smallest of these two values were then determined and the value was denoted by dt . The next earthquake event was then produced by adding the additional stress arising in the time dt to $f_{i,j}$. Hence if a cell was empty of magma, the stress added was determined by

$$f = f + dt, \quad (6.3)$$

and for the cells filled with magma,

$$f = f + (1 + \delta) \times dt. \quad (6.4)$$

After implementing these concepts, it was then possible to analyse the model in order to test the impact these changes had. This required checking the efficiency of the model against well known physical properties of volcanic activity.

6.3 Implications to Eruption Statistics

Simulating the model, using the method above with the new stress property, the results for the probability density, time and maximum water content were observed. Most interesting perhaps is the effect this property has on the probability density of eruptions of given sizes for varying values of δ . In Figure 21 it is observed that a power law distribution is maintained regardless of the values of δ ranging from 0.1–0.6 respectively. In comparison with Figure 12 which shows the probability density setting $\delta = 0$, a bulge of larger events can be seen with a higher frequency. Also of note is the length of the power law region. As δ increases, the range of the power law decreases. For example for $\delta = 0.1$ the power law extends as far as ≈ 2.2 ; where as for $\delta = 0.6$ it is ≈ 1.8 .

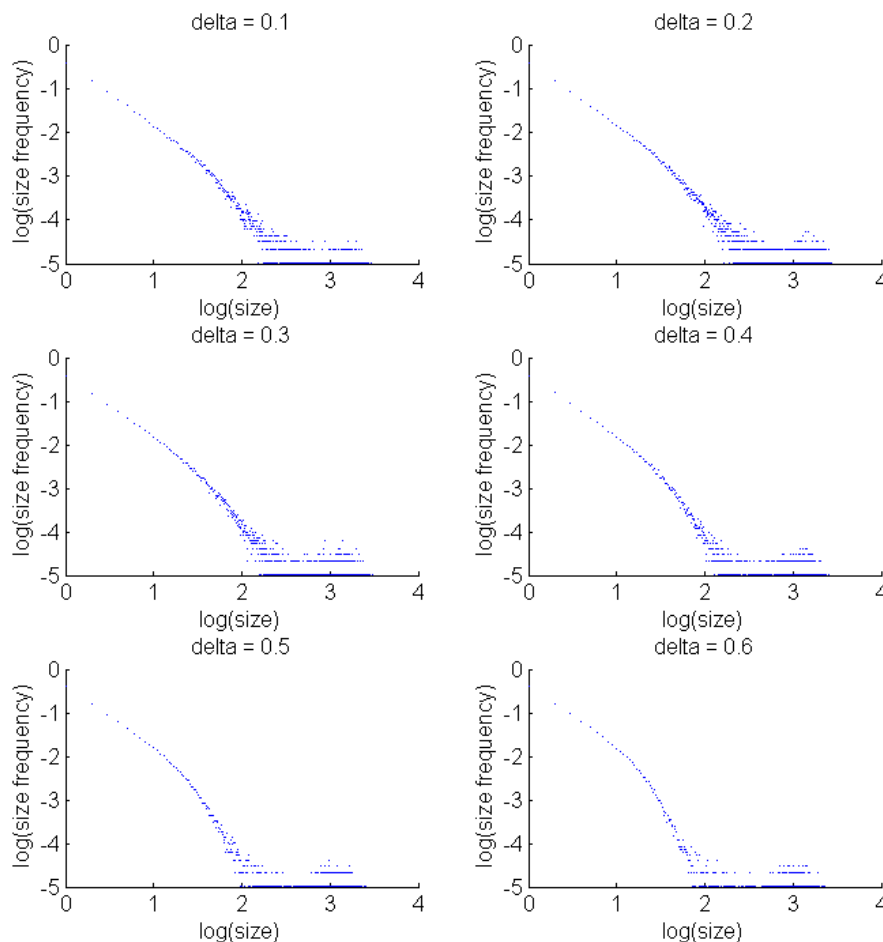


Figure 21: Probability distribution for simulated eruptions, varying the value of δ , using data from 10^6 eruptions.

By exerting an additional stress onto those cells filled with magma, there is an increase in the likelihood of those cells fracturing again in the next “earthquake” event. Once magma has moved into a fractured cell and the stress level of that cell is reset to zero, in the model discussed in the previous sections, it would take a longer time for this cell to become fractured again, as the perturbations applied to the model are constant across the whole of the grid. In this model however, the likelihood of that same cell becoming fractured again due to the presence of magma is increased depending on the value of δ . This will lead to an increased likelihood of large events since clusters of cells containing magma all have an increased stress rate, and therefore are considerably more likely to trigger a new earthquake event, or be involved in one following the distribution of stress to neighbouring cells via the rules shown in Figure 2. If the cells that contain magma are more prone to becoming fractured, there is therefore an increased probability of much larger events occurring.

Similarly, if the inter-eruption times are considered at the extremes, $\delta = 0.1$ and $\delta = 0.6$, a noticeable difference appears; see Figure 22.

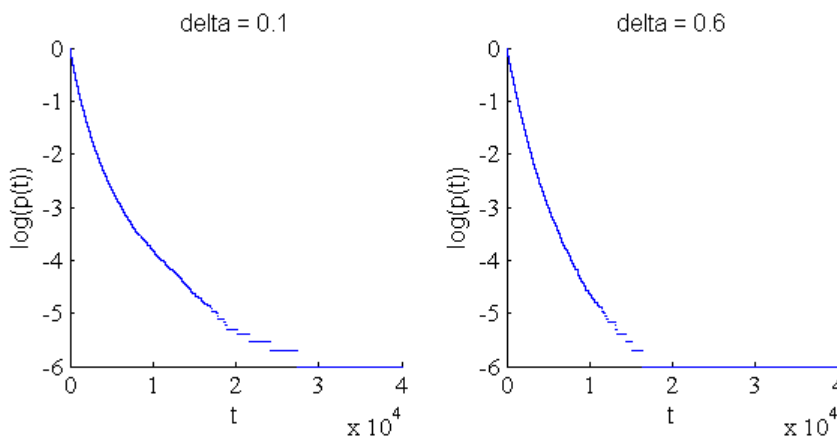


Figure 22: The cumulative probability distribution of inter-eruption times for simulated eruptions, varying the value of δ and using data from 10^6 eruptions.

For large values of δ , there is a far larger probability of having a short span of time between events, than that produced by using small values of δ . In a sense this seems logical, since the addition of more stress onto cells containing magma will result in higher values of the $maxval(f)$, as discussed in Section 2.2, and hence smaller values of $1 - maxval(f)$, resulting in much shorter inter-eruption times. On the other hand, Figure 21 shows that an increase in δ leads to a greater occurrence of larger events, which often occur following long periods of inactivity. From this latter factor alone, it might be expected that larger inter-eruption times are more common for large values of δ . It would appear, however, that the additional stress plays a much larger role, thus producing the behaviour seen in Figure 22.

6.4 Implication on the Stress Field

The aim of this section is to analyse the impact this additional stress has on the distribution of fractures across the grid (size 64×64). In order to determine this, the number of times a cell becomes fractured during a run of 10^6 eruptions, is recorded, and the results for the original model and the new model are compared.

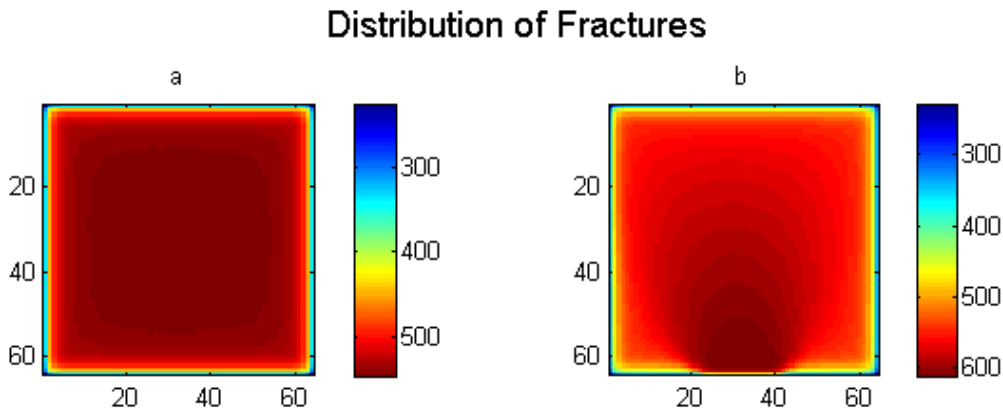


Figure 23: Distribution of Fractures across the grid - (a) representing a simulated model without imposing additional stress on cells containing magma, (b) representing a simulated model with the additional stress on magma cells. The numbers on the colour bar correspond to thousands of fracture events.

Figure 23(a) shows the distribution of the fracture events across the grid, with only shear stress being taken into account. It shows that the distribution of stress is spread evenly around the grid, which was to be expected given the initial random configuration of the OFC model and the subsequent constant drive. The cells on the corners have a lower probability of being fractured, closely followed by those at the edge, due to the non-conservative nature of the boundary conditions being implemented. In contrast the results of Figure 23(b), which shows the distribution of fracture events with the additional stress added in by the presence of magma, shows that the cells within the lower central section of the grid have a higher probability of being fractured. Physically speaking, stress being applied constantly results in repeated failure, known as static fatigue. This is a commonly known property of materials such as rock^[22] and so therefore an increase in this stress in certain sections of the grid, will lead to a higher concentration of fractures in that area, as can be seen above. The significance of this will be tested when cross examined with the magma field, as to the location and movement of magma.

The reason behind the preference for fractured cells occurring towards the centre of the grid, is that when magma does rise into the system from the reservoir, it primarily resides directly above the middle quarter of the grid. Therefore when the system stops and the stress is recalculated, it makes sense that these cells subsequently feel the effect of the additional stress imposed by the magma. Previous numerical checks made by Piegari *et al.* on the model determined that the size of the opening to the magma reservoir did not alter the statistical properties of the model.^[18] However, with the addition of this new development the choice of the size of this opening at the bottom of the grid must be taken into consideration and analysed. An interesting area to consider in future work on this model, would be the impact of increasing the size of this connection to the central reservoir and determining the effects this has on the model.

6.5 Subsequent Implications on the Magma Field

The imposed condition regarding the axial symmetry of the model, as described in Section 4.4, was removed prior to observing the distribution of magma. Whilst monitoring the distribution of fractures across the grid, every time a new set of fractures appeared in the rock, and magma had the potential to move within the system, the distribution of magma across the grid was recorded. Figure 24 shows the distribution of magma for both the original model (a) and the new model (b).

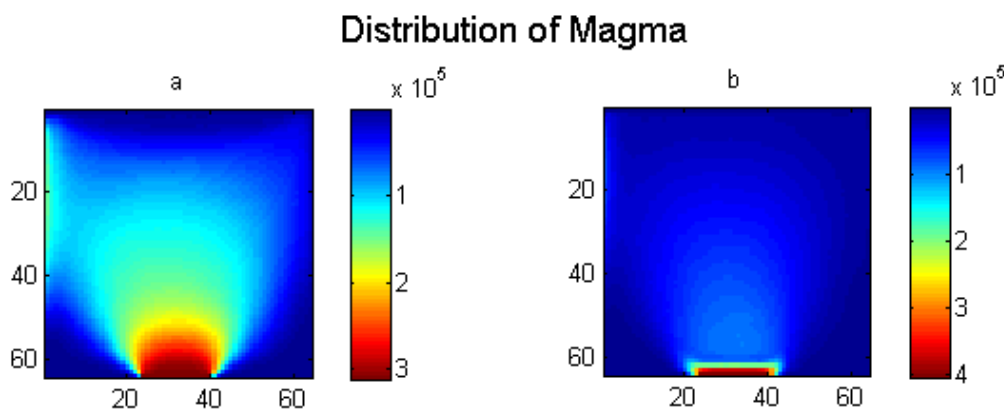


Figure 24: Distribution of Magma across the grid - (a) representing a simulated model without imposing additional stress on cells containing magma, (b) representing a simulated model with the additional stress on magma cells. The numbers on the colour bar correspond to thousands of fracture events.

From Figure 24 key similarities and key differences can be seen between the 2 models.

- Similarities** - In both the grids above, magma is rarely present in the bottom left and right hand corners of the grid. This result is to be expected due to the probabilistic nature of the horizontal movement within the algorithm. Another similarity is that at the top of the grid, the magma has a smaller probability of being present; this is because an eruption will often occur, removing the magma from these cells. As can be seen previously, the most common eruptions are those with a high gas loss, resulting in effusive eruptions and therefore it is these cells that will lose the magma present more often.
- Differences** - The major difference between the 2 grids is the spread of magma across the centre. In Figure 24(a) it appears to form a v-shape, spreading out across the whole grid. In contrast Figure 24(b) shows a central preference, with the area more likely to contain magma being along a central channel.

A slight concern in these results is the shift in distribution towards the top left hand corner of the grid, a characteristic present in both models. However, one potential explanation is that this is the result of the algorithm looping over the magma cells on a left to right basis, resulting in a slight net preference for motion to the left. In order to test,

understand and hopefully overcome this apparent discrepancy it would be advisable to run the simulation again, restricting the movement of magma back into a cell it has just vacated during each horizontal loop of the magma algorithm (Figure 7). Alternative grid sizes should also be considered since the figures above are created on a grid size of 64×64 , which may not be large enough to exclude the effect of the applied boundary conditions.

In Section 4.4 and the 2011 paper by Piegari *et al.* an axial symmetry was applied to the model manually through the adaptation of the algorithm in Figure 7. This was due to the physical property that in many cone-shaped volcanoes, the magma chamber favours a central path. Figure 25 shows the likelihood of magma in each of the cells of the grid being involved in an eruption, with the blue end of the scale representing the least likely and the red, the most likely.

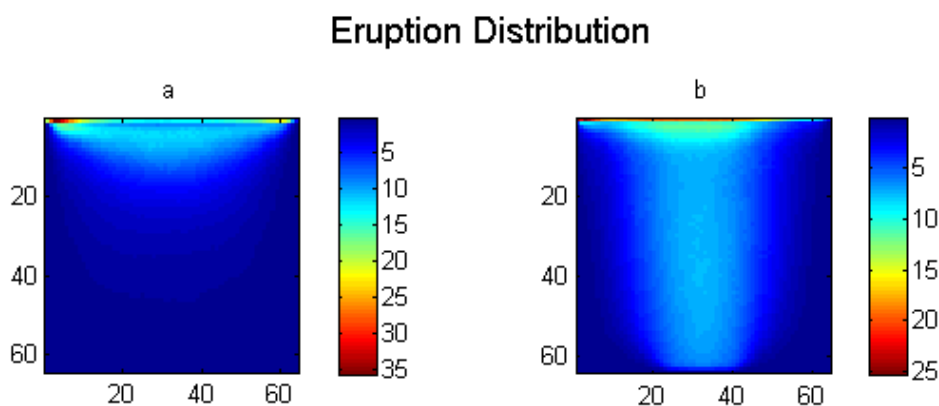


Figure 25: Distribution of the Magma involved in an eruption across the grid - (a) representing a simulated model without imposing additional stress on cells containing magma, (b) representing a simulated model with the additional stress on magma cells. The numbers on the colour bar correspond to thousands of eruptions.

This figure shows a natural preference to a central path, produced by the additional stress of the magma onto the walls of the magma chamber. Not only does this alleviate the need to impose an axial symmetry on the grid, it uses a well known physical property of magma that imposes the property naturally. In the VEI index, volcanoes favouring central craters make up 61% of volcanoes in the list,^[2] and so in future work this model could be applied to, and focused on, volcanoes such as those. Relating this analysis to the result that an increase in δ leads to larger eruptions more commonly occurring, as shown in Figure 21, this makes sense. In Figure 25(a) where the distribution of magma cells involved in an event is largely congregated in the top sixth of the grid, it would be expected that the most common eruptions are of small size. On the other hand, the distribution shown in Figure 25(b) shows a much wider spread of distribution showing that, in comparison to the other grid, cells lower down are much more likely to be involved in an event, hence resulting in eruptions of much larger size.

7 Conclusions and Future Directions

This report has reviewed, analysed and developed the recent model produced by Piegari *et al.* with a focus on the mathematical properties of the model relating to volcanic activity. Having written the computer model replicating the results of Olami, Feder and Christensen, Chapter 2 focused on verifying results in the literature, in order to use this as the underlying model upon which the volcano model was later produced. Following this work, it was then possible to alter and adapt the computer code to incorporate the addition of a magma, reproducing and identifying significant results from both the 2008 and 2011 papers by Piegari *et al.* This background investigation, and the code produced, facilitated further consideration of the model and the implementation of a further and more detailed analysis of the interaction between the magma and stress fields. These results were then analysed and cross examined against known physical properties of volcanoes, and the outcomes of this advancement to the model were then presented in Section 6.

Throughout the work on this model, a few discrepancies occurred when reproducing some of the work by Piegari *et al.* Contact was made with the first author and some of these discrepancies were successfully addressed, allowing for an update of the model, based on their feedback. However, in some cases there remained difficulties in replicating the precise numerical results from the Piegari model. Nevertheless, the patterns obtained from the current model, such as the power law clearly displayed in the probability density of eruptions of given size, were in keeping both with Piegari's results and the patterns shown in numerical data from volcanic statistics. In their 2008 paper, Piegari *et al.* recognised that “*a quantitative comparison with our probability distribution can not be made*” and therefore we concluded that our model was working efficiently, despite the lack of exact numerical agreement.

Section 6 sets out the details of the advancement made to the Piegari model. Neither new statistics nor laws regarding volcanic eruptions were discovered, although the results of Figure 21 do show small variations of the power law; rather the key finding was the effect the dependence between the magma and stress fields had on the interior of the magma chamber. The results negated the need to implement an imposed axial symmetry on the magma field, since incorporating this physically appropriate variable in the model produced a central conduit naturally. This is important for future work, since over 61% of volcanoes display this phenomena.

Prior to a paper being written on the findings of Section 6, the results of longer runs must be obtained and analysed to further verify the results achieved. In addition the width of the reservoir warrants further consideration, and a check made for the consistency of the results for varying widths. However, the results so far support the intuitive idea of a central conduit within the magma chamber. Once these results have been verified, a radial stress zone would be the next obvious step to consider, as this would produce a

more physically precise adaptation of the model.

In light of the results obtained, the works undertaken have made significant adaptations to the Piegari model, which could be implemented in the development of future work in this field. It is considered that the findings of the report add to the knowledge base and will assist in developing further understanding of some of the physical properties of volcanoes. Given the impact of major volcanic eruptions and the large numbers of people living in close proximity to volcanoes, any advancement in understanding and in the ability to predict major events will be of benefit.

References

- [1] E.Piegari, V.Cataudella, R.Di Maio, L.Milano, M.Nicodemi, R.Scandone, 2008. A model of volcanic magma transport by fracturing stress mechanisms, *Journal of Volcanology and Geothermal Research*. Vol 202. p22-28
- [2] L.Siebert, T.Simkin, P.Kimberly, 2010. *Volcanoes of the world*, III edition. Smithsonian Institution, University of California Press. London. p1-17
- [3] P.Bak, C.Tang, K.Wiesenfeld, 1988. Self-Organised Criticality. *Physical Review. A*. Vol 38. Number 1. p364-374
- [4] Z.Olami, H.Feder, K.Christensen, 1992. Self-Organised Criticality in a continuous, Non-Conservative Cellular Automaton Modelling Earthquakes. *Physical Review Letters*, Vol 68. Number 8. p1244-1247
- [5] J.Huang, G.Narkounskaia, D.L.Turcotte, 1992. A cellular-automata, slider-block model for earthquakes II, Demonstration of self-organised criticality for a 2-D system, *Geophysical Journal International*. Vol 111. p259
- [6] H.Jensen, 1998. *Self-Organised Criticality- Emergent Complex Behaviour in Physical and Biological Systems*. Cambridge University Press. p49
- [7] I.G.Georgoudas, G.Sirakoulis, I. Andreadis, 2006. Modelling Earthquake Activity features using Cellular Automata. *Mathematical and Computer Modelling*, Vol 46, p124-137
- [8] P. Sarkar, 2000. A Brief History of Cellular Automata. *ACM Computing Surveys*. Vol 32, p 80-82
- [9] National Research Council, 2003. *Living on an Active Earth: Perspectives on Earthquake Science*. The National Academies Press. Washington, DC. p260
- [10] E.Preston, J.Martins, J.Rundle, M.Anghel, 2000. Models of Earthquake faults with long-range stress transfer. *Computing in Science and Engineering*. Vol 2. Issue 3. p34-36
- [11] K.Christensen and Z.Olami, 1992. Scaling, phase transitions and non-universality in a self-organised critical cellular-automaton model. *Physical Review*. Vol 46. Number 4. p1829-1838
- [12] K.Nakamura, K.Jacob, J. Davis, 1977. Volcanoes as possible indicators of tectonic stress orientation - Aleutians and Alaska. *Pure and Applied Geophysics*. Vol 115. Issue 1-2. p 87-112
- [13] R.Scandone, L.Giacomelli, F.Fattori Speranza, W.Plastino, 2009. Classification and quantification of volcanic eruptions. *Bollettino di Geofisica Teorica ed Applicata*. Vol 50. Issue 2. p103-116

- [14] E.Piegari, R.Maio, R.Scandone, 2011. Effects of different rock density profile on magma ascent and on the statistical distributions of simulated eruptions. *Bollettino di Geofisica Teorica ed Applicata*. Vol 53. Issue 4. p551-558
- [15] L.Wilson, R.Stephen, J.Sparks, G.Walker, 1980. Explosive Volcanic Eruptions - The Control of Magma Properties and Conduit Geometry on Eruption Column Behaviour. *Geophysical Journal of the Royal Astronomical Society*. Vol 63. Issue 1. p117-148
- [16] C.H.Newhall, S.Self, 1982. The Volcanic Explosivity Index (VEI): An estimate of Explosive Magnitude for Historical Volcanism. *Journal of Geophysical Research*. Vol 87. Issue C2. p1231-1238
- [17] E.Piegari, R.Di Maio, R.Scandone, 2013. Analysis of the Activity Pattern of Volcanoes through Self-Organised Crack Networks: The effect of density barriers- An application to Vesuvius Activity in the Period 1631-1944. *Earth and Planetary Science Letter*. Vol 371-371. p269-277
- [18] E.Piegari, R.Maio, R.Scandone, L.Milano, 2011. A Cellular Automaton Model for Magma Ascent: Degassing and Styles of Volcanic Eruptions. *Journal of Volcanology and Geothermal Research*. Vol 202. Issues 1-2. p22-28
- [19] P.Papale, 1999. Strain-induced magma fragmentation in explosive eruptions. *Letters to Nature*. Vol 397. p425
- [20] H.Schmincke, 2004. *Volcanism*. Springer-Verlag Berlin Heidelberg. New York. p239
- [21] R.Das, Y.Zhang, P.Schaubs, P.W.Cleary, 2014. Modelling Rock Fracturing Caused by Magma Intrusion using the Smoothed Particle Hydrodynamics Method. *Computational Geosciences*. Vol 18. Issue 6. p927-947
- [22] C.R.J Kilburn, 2003. Multiscale Fracturing as a Key to Forecasting Volcanic Eruptions. *Journal of Volcanology and Geothermal Research*. Vol 125, Issues 3-4. p271-289